Solvent-Free Synthesis of SAPO-34 Zeolite with Tunable SiO₂/Al₂O₃ Ratios for Efficient Catalytic Cracking of 1-Butene

Xia Xiao [1], Zhongliang Xu [1], Peng Wang [1], Xinfei Liu [1], Xiaoqiang Fan [1], Lian Kong [1], Zean Xie [1] and Zhen Zhao [1,2,*]

[1] Institute of Catalysis for Energy and Environment, College of Chemistry and Chemical Engineering, Shenyang Normal University, Shenyang 110034, China; xiaoxia@synu.edu.cn (X.X.); xuzhongliangcup@126.com (Z.X.); pengw0511@163.com (P.W.); liuxinfei0825@126.com (X.L.); fanxiaoqiang@synu.edu.cn (X.F.); konglian@synu.edu.cn (L.K.); xiezean@synu.edu.cn (Z.X.)

[2] State Key Laboratory of Heavy Oil Processing, China University of Petroleum, Beijing 102249, China

* Correspondence: zhenzhao@cup.edu.cn; Tel.: +86-24-86579800

Abstract: Solvent-free synthesis methodology is a promising technique for the green and sustainable preparation of zeolites materials. In this work, a solvent-free route was developed to synthesize SAPO-34 zeolite. The characterization results indicated that the crystal size, texture properties, acidity and Si coordination environment of the resulting SAPO-34 were tuned by adjusting the SiO_2/Al_2O_3 molar ratio in the starting mixture. Moreover, the acidity of SAPO-34 zeolite was found to depend on the Si coordination environment, which was consistent with that of SAPO-34 zeolite synthesized by the hydrothermal method. At an SiO_2/Al_2O_3 ratio of 0.6, the SP-0.6 sample exhibited the highest conversion of 1-butene (82.8%) and a satisfactory yield of light olefins (51.6%) in the catalytic cracking of 1-butene, which was attributed to the synergistic effect of the large S_{BET} (425 m^2/g) and the abundant acid sites (1.82 mmol/g). This work provides a new opportunity for the design of efficient zeolite catalysts for industrially important reactions.

Keywords: solvent-free synthesis; SAPO-34; SiO_2/Al_2O_3 molar ratios; 1-Butene catalytic cracking; light olefins

1. Introduction

The SAPO-34 silicoaluminophosphate zeolite, which contains a large chabazite (CHA) cage and an eight-ring pore opening, has attracted tremendous interest from various industries as a catalyst and sorbent [1–6]. The acidity of this zeolite catalyst can be modified to improve product selectivity and restrain carbon deposition [7–10]. The Brønsted acidity of the SAPO-34 zeolite is typically generated by the bridging hydroxyl group (Si–OH–Al), which originates from protons that offset the unbalanced electric charges; this is closely related to the introduction of Si atoms into neutral $AlPO_4$-34 frameworks [11–13]. Considering the effect of the incorporation of Si atoms into aluminophosphate (AlPO) frameworks on the Brønsted acidity of SAPO-34, significant attention has been paid to studying the substitution mechanism of Si atoms' incorporation into these AlPO frameworks [9,12,14,15].

Two different substitution mechanisms for Si-atom incorporation into the AlPO4-34 structure have been proposed to date [13,15]. The SM2 substitution mechanism involves the replacement of phosphorus with silicon to form Si(4Al) structures, resulting in a Brønsted acid sites at each substitution centre [13]. The SM3 mechanism involves the simultaneous double substitution of neighbouring aluminium and phosphorous atoms with two silicon atoms to form Si(3Al), Si(2Al), Si(1Al), and Si(0Al) structures, resulting in the formation of stronger Brønsted acid sites [13]. In addition, if the Si content of the SAPO-34 framework is at a threshold value, the SM2 and SM3 mechanisms occur simultaneously to generate Si islands, and do not produce new acid sites. The amount and distribution of Si atoms in these frameworks is known to be closely related to the structure, acidity, and catalytic performance of the SAPO-34 zeolite synthesised via the conventional

hydrothermal route [11,13,14]. Therefore, establishing the relationship between the Si substitution mechanism, Si content, and acidity of SAPO-34 is crucial.

Solvent-free synthesis of zeolites has attracted considerable recent attention owing to its advantages over traditional hydrothermal (or solvothermal) synthesis of zeolites [16–20]. Xiao et al. developed a solvent-free route for the synthesis of the SAPO-34 silicoaluminophosphate zeolite by mechanically mixing solid raw materials, followed by heating in a closed vessel; this was found to significantly increase the product yield, effectively eliminate the unsafe high pressure, and making the synthesis green and sustainable [16,18,19]. Solvent-free synthesis is also a particularly facile method for constructing hierarchical SAPO-34 zeolites in the absence of expensive templates [16,18,20]. Hetero-atom incorporation into the SAPO framework plays a major role in influencing the coordination states of Si and, consequently, the acidic properties of the resulting MeAPSO samples [12]. Si-, Co-, and Mg-substituted aluminophosphate zeolites with AEL and AFI structures [19], and Mg-incorporated SAPO-34 zeolites [21], have recently been developed using the solvent-free method. Unlike hydrothermal synthesis, solvent-free synthesis is a promising technique with respect to the green preparation of zeolites. Although the mechanism of Si-atom incorporation into zeolite frameworks via hydrothermal crystallization has been reported in previous studies, intimate knowledge of the mechanism of Si-atom incorporation into zeolite frameworks and the acidity of SAPO-34, obtained via solvent-free synthesis, is lacking. These observations motivated us to investigate the mechanism of the incorporation of Si into SAPO-34 crystals obtained through solvent-free synthesis.

Light olefins such as ethylene and propylene are important building blocks of the petrochemical industry. Recently, driven by the increasing demand for polyethylene and polypropylene, some industrial pathways such as methanol-to-olefins [1,14,22], catalytic cracking of hydrocarbons [23,24], light alkanes dehydrogenation [25,26] and Fischer–Tropsch to olefins [27,28] have attracted much attention. Among them, the catalytic cracking of butene to propene in the presence of a highly effective catalyst is considered one of the most attractive approaches. Despite these remarkable achievements, the application of a SAPO-34 catalyst synthesized by the solvent-free method in the catalytic cracking of butene reaction has been seldom reported to date.

In this study, the effect of the SiO_2/Al_2O_3 molar ratio in the starting mixture on the physicochemical properties of the obtained SAPO-34 crystals, including the crystal size, texture properties, acidity, and Si chemial coordination environment in the zeolite framework, were systematically investigated. The chemical environment of Si and mechanisms of Si-atom incorporation into the SAPO-34 framework were analyzed by adjusting the SiO_2/Al_2O_3 molar ratio. SAPO-34 samples with decent crystallinity, large specific surface area, and improved catalytic activity were obtained when the SiO_2/Al_2O_3 molar ratio was within an appropriate range. This work shed light on how to optimize the catalytic performance for the 1-butene catalytic cracking reaction of SAPO-34 zeolite by adjusting the silicon content in the composite template system via a solvent-free route. This study will facilitate understanding of the solvent-free synthesis of various silicoaluminophosphate materials in promoting industrially important reactions.

2. Results and Discussion

2.1. Catalyst Characterization

2.1.1. The Structural and Chemical Compositions of SAPO-34 Zeolite

The X-ray diffraction (XRD) patterns of the as-synthesised SAPO-34 samples are shown in Figure 1. The XRD patterns of the SP-0.0 sample do not appear to exhibit characteristic peaks in SAPO-34, indicating its amorphous nature. The XRD patterns of all the samples, except for SP-0.0 sample, show peaks at 2θ = 9.6°, 16°, 20.5°, 26° and 31°, which are assigned to the diffraction of the silicoaluminophosphate analogue of the CHA structure (PDF#47-0168) without obvious impurities and no indication of amorphous; this observation agrees with the commercial SAPO-34 (Figure S1, left) and the previously reported results [18]. However, a significant variation in crystallinity is clearly visible. The relative crystallinity

of the SAPO-34 samples first increases and subsequently decreases with an increase in the SiO_2/Al_2O_3 ratio, and the peak intensities of the SP-0.6 sample are evidently higher than those of the other samples, revealing its considerably high crystallinity.
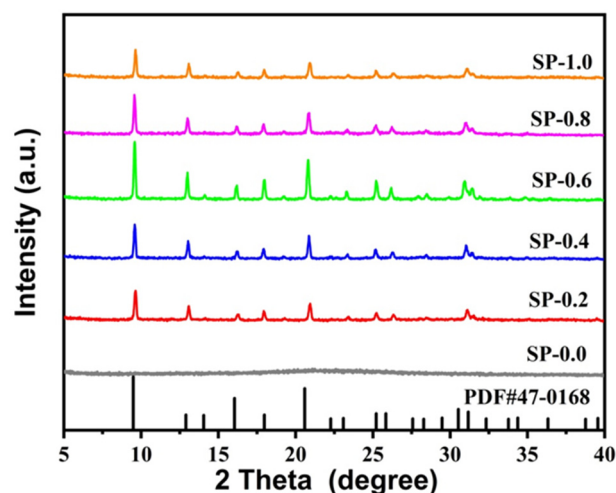

Figure 1. XRD patterns of as-synthesized samples.

The incorporation of Si into the SAPO-34 framework is closely related to the generation of Brønsted acid sites [9,14]. The Si content of SAPO-34 directly affects the acidic properties of the samples [12,22]. Therefore, X-ray fluorescence (XRF) was employed to obtain the chemical composition of the samples, as shown in Table 1. For the samples prepared with an increase in fumed silica content, the ratios of $Si/(Si + Al + P)$ in the samples gradually increase in the following order: SP-0.2 < SP-0.4 < SP-0.6 < SP-0.8 < SP-1.0. The synthesis of pure SAPO-34 with a low content of Si [$Si/(Si + Al + P) < 0.07$] was challenging in terms of solvent-free synthesis [13]. The possible substitution mechanisms of Si incorporation into AlPO structures will be discussed later.

Table 1. Compositions of the as-synthesized samples.

Samples	x(SiO_2)	Molar Composition [1]	Si/(Si + Al + P)
SP-0.2	0.2	$Al_{0.338}Si_{0.042}P_{0.620}O_2$	0.042
SP-0.4	0.4	$Al_{0.290}Si_{0.053}P_{0.657}O_2$	0.053
SP-0.6	0.6	$Al_{0.284}Si_{0.074}P_{0.642}O_2$	0.074
SP-0.8	0.8	$Al_{0.290}Si_{0.095}P_{0.615}O_2$	0.095
SP-1.0	1.0	$Al_{0.246}Si_{0.127}P_{0.627}O_2$	0.127

[1] Measured by XRF.

2.1.2. The Morphology of SAPO-34 Zeolite

The corresponding scanning electron microscopy (SEM) images of the samples are presented in Figure 2. The SP-0.0 sample exhibits an extremely uniform rhombohedral morphology with a particle size of approximately 2–3 μm. The SEM and XRD analyses indicate that these rhombohedral particles represent amorphous phosphoaluminates corresponding to the SAPO-34 precursor. As shown in Figure 2b, the SP-0.2 sample consists of mixed aggregates of uniform cube-like and rhombohedral crystals, with a typical cube-like-particle size of approximately 3–4 μm. The commercial SAPO-34 also possesses a cubic morphology (Figure S1, right). As the Si content in the synthesis recipe increases, the content of the amorphous rhombohedral phosphoaluminate reduction and the crystal grain size increases. As shown in Figure 2c–f, the SP-0.4, SP-0.6, SP-0.8, and SP-1.0 samples also exhibit a mixed rhombohedral and cubic morphology, with the cubic particles of SAPO-34 increasing in size from 4 μm to 10 μm. It is particularly interesting to note that the surface of the SP-0.8, and SP-1.0 samples becomes extremely rough, with tiny crystals,

and the morphology becomes irregular, indicating the reduction in crystallinity; this is consistent with the XRD results. The SEM results demonstrate that the SiO_2/Al_2O_3 ratio affects the crystal size and morphology of SAPO-34. Additionally, the transformation of the rhombohedral amorphous phosphoaluminate precursor to the cubic SAPO-34 crystals via solvent-free synthesis is confirmed.
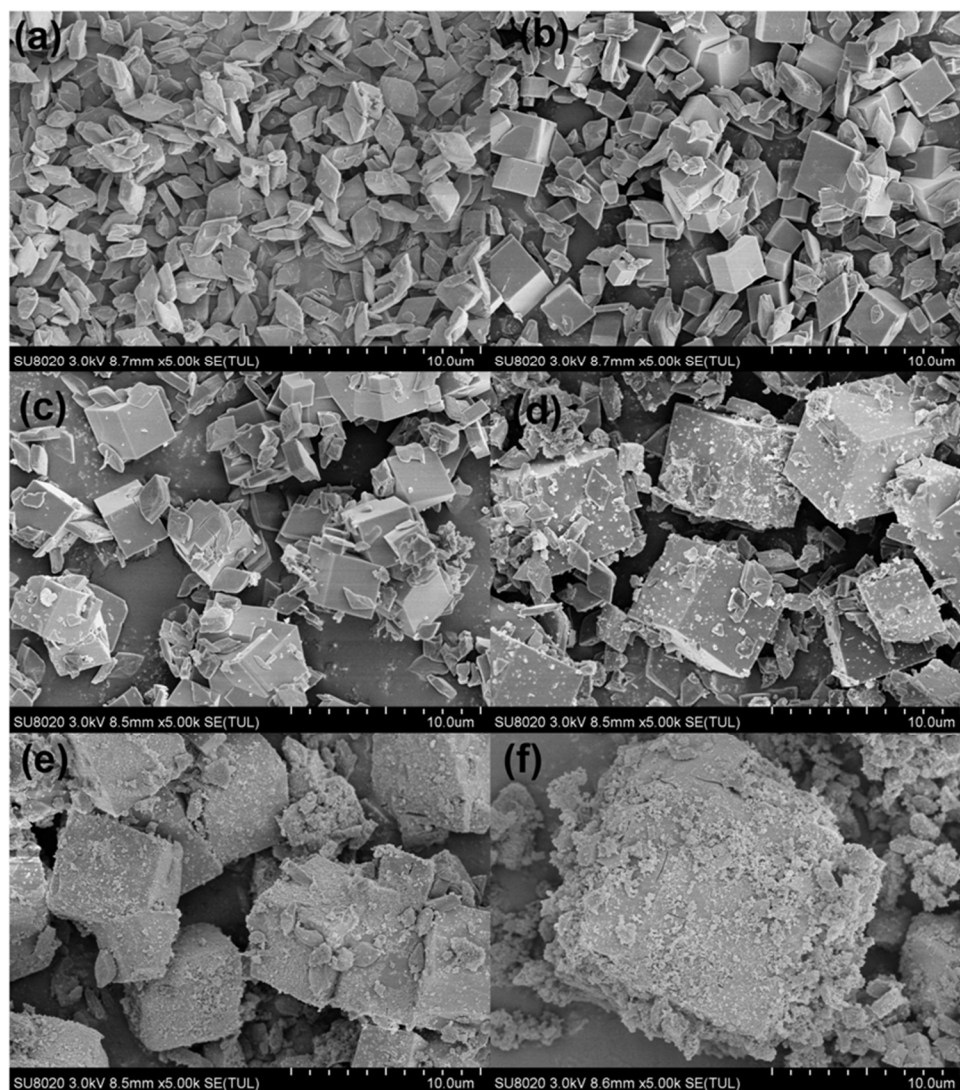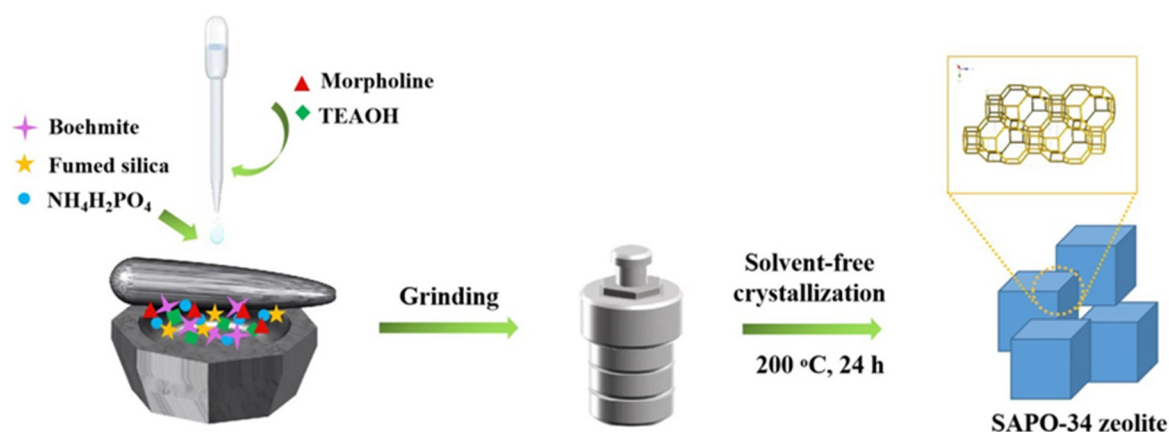

Figure 2. SEM images of as-synthesized samples: (**a**) SP-0.0; (**b**) SP-0.2; (**c**) SP-0.4; (**d**) SP-0.6; (**e**) SP-0.8; (**f**) SP-1.0.

Scheme 1 illustrates the construction of SAPO-34 crystals, synthesized by the solvent-free synthesis method, with the TEAOH and MOR as dual-template agents. The synthesis can be divided into two main steps: (i) the formation of amorphous raw materials mixture powder by grinding; (ii) induced nucleation and the production of a high number of SAPO-34 zeolite crystals by high-temperature crystallization treatment. Thus, it can be seen that the solvent-free route with sustainable features is an environmentally benign, simple and efficient synthesis strategy of SAPO-34. In addition, this method has some advantages, such as high space–time yields, low wastes, low pressure and fast crystallization, compared to the traditional hydrothermal synthesis methodology [16].

Scheme 1. Schematic representation of the formation of SAPO-34 zeolite.

2.1.3. The Textural Properties of SAPO-34 Zeolite

Figure 3 shows the N_2 adsorption–desorption isotherms of the prepared samples. All the samples are observed to exhibit a steep increase in the relative pressure range of $10^{-6} < P/P_0 < 0.01$, confirming the microporosity of the samples. Moreover, a hysteresis loop in the relative pressure region of $0.45 < P/P_0 < 0.98$ can be observed, indicating the presence of mesopores. The synthesis of hierarchical SAPO-34 without a mesoporous template via solvent-free synthesis emphasises its environmental friendliness and inexpensiveness. The results also confirm that the hierarchical structure of the SAPO-34 samples is possibly related to the transformation of the solid porous starting materials into zeolite crystals [18]. Similar experimental phenomena have been observed in MFI zeolites obtained via solvent-free synthesis [16]. Pore size distribution shows the presence of mesopores from 10 to 50 nm; however, the SP-0.8 and SP-1.0 samples have larger mesopores, which should come from the transformation of the solid porous starting materials into zeolite crystals. Furthermore, the texture data in Table 2 indicate the existence of a mesoporous structure in the as-synthesised SAPO-34 samples. The Brunauer–Emmett–Teller (BET) surface area and micropore volume of the SAPO-34 samples increases, and subsequently decreases with an increase in the SiO_2/Al_2O_3 molar ratio. The BET surface area and micropore volume of the SP-0.6 sample (425 m^2/g and 0.21 cm^3/g, respectively) are evidently higher than those of the other samples. The BET surface area and micropore volume of SP-0.8 and SP-1.0 are seen to decrease, owing to the decrease in crystallinity and increase in crystal size. Therefore, the XRD, SEM, and N_2 adsorption–desorption analyses proved that the SAPO-34 zeolite with decent crystallinity was successfully prepared using a moderate amount of Si through a solvent-free method.

Table 2. Textural properties of as-synthesized samples.

Samples	S_{BET} [1] (m^2/g)	S_{micro} [2] (m^2/g)	S_{ext} [3] (m^2/g)	V_{micro} [4] (cm^3/g)	V_{meso} [5] (cm^3/g)
SP-0.2	224	204	20	0.11	0.02
SP-0.4	326	299	27	0.16	0.03
SP-0.6	425	410	15	0.21	0.02
SP-0.8	395	363	32	0.19	0.06
SP-1.0	358	329	29	0.17	0.09

[1] S_{BET} was determined by BET equation. [2] S_{micro} determined from the t-plot method. [3] $S_{ext} = S_{BET} - S_{micro}$. [4] V_{micro} and [5] V_{meso} were determined by t-plot method.
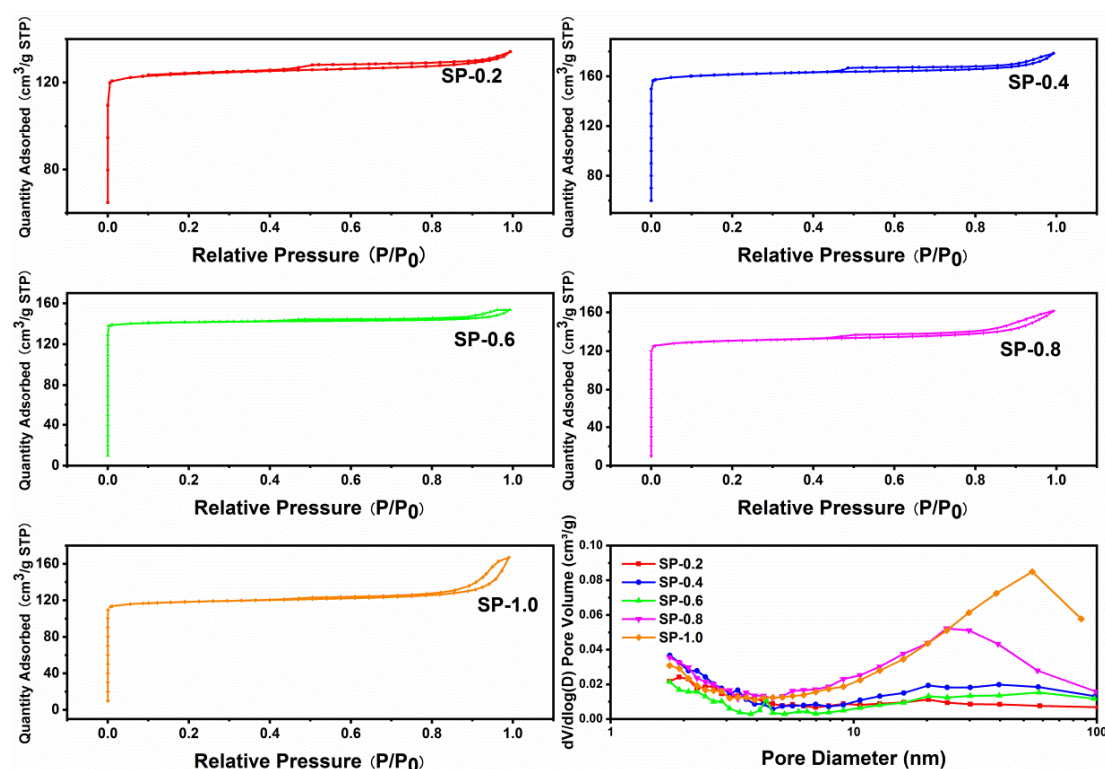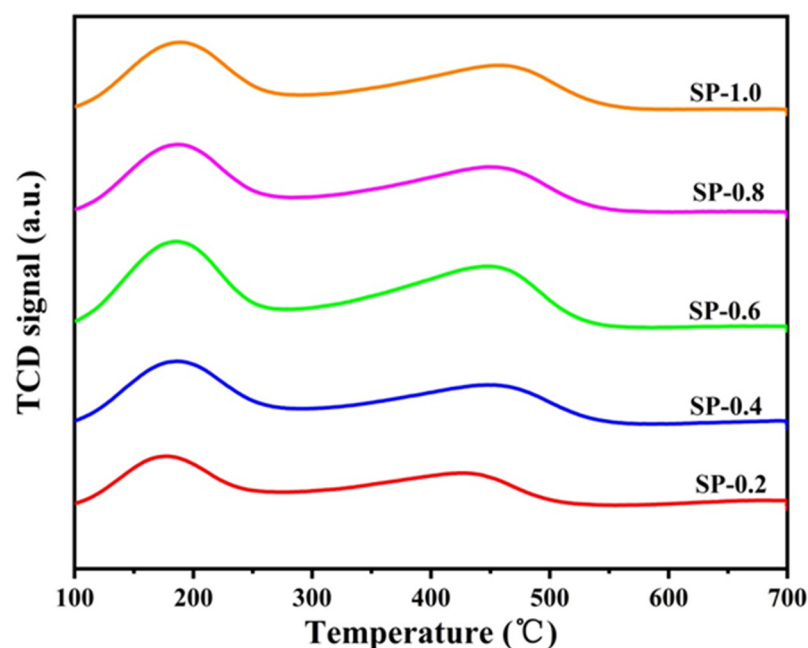
Figure 3. N_2 adsorption–desorption isotherms and BJH pore size distribution of as-synthesized samples.

2.1.4. The Acid Properties of SAPO-34 Zeolite

Temperature-programmed desorption with ammonia (NH_3-TPD) was employed to characterise both the acidic concentration and strength of all the as-synthesised SAPO-34 samples [15]. The densities of the acid sites of all the samples are listed in Table 3. As shown in Figure 4 and Table 3, all samples show two distinct desorption peaks at ~190 and 450 °C, which correspond to NH_3 desorption from weak and strong acid sites, respectively [9]. With an increase in the SiO_2/Al_2O_3 ratio, all the high-temperature peaks were noted to shift to higher temperatures, indicating a slight increase in the strength of the strong acid sites; the strength of the weak acid sites of all the samples remained unchanged. The acidity of SAPO-34 is known to vary in accordance with its Si content [15]. Table 3 indicates that the relationship between the acidic content and SiO_2/Al_2O_3 ratio is not straightforward. The total acidic content increases from 1.51 mmol/g (SP-0.2) to a maximum of 1.82 mmol/g (SP-0.6), and subsequently decreases to 1.75 mmol/g (SP-1.0). These results may be attributed to the control of the acidic content of SAPO-34 by at least two different substitution mechanisms with respect to the incorporation of Si into the zeolite framework [14]. When the SiO_2/Al_2O_3 ratio is less than 0.6, the acid content significantly increases with increasing contents of Si, because more Si is incorporated into the AlPO framework to generate more Brønsted acid sites. However, when the SiO_2/Al_2O_3 ratio is greater than 0.6, the acidic content slightly decreases with an increase in the Si content, because of the possible formation of Si islands and the lack of generation of new acidic sites [12,13,15]. Generally, SAPO-34 catalysts with a mild acid strength and a relatively low density of acidic sites are preferable for the catalytic cracking of 1-butene [23].

Table 3. The amount of acid sites of as-synthesized samples.

Samples	Acid Amount (mmol/g)			Desorption Temperature (°C)	
	Total Acid Amount	Weak Acid Amount	Strong Acid Amount	Low Temperature	High Temperature
SP-0.2	1.51	0.77	0.74	184	435
SP-0.4	1.54	0.78	0.76	187	441
SP-0.6	1.82	0.89	0.93	188	452
SP-0.8	1.76	0.87	0.89	186	457
SP-1.0	1.75	0.87	0.88	188	465

Figure 4. NH_3-TPD curves of as-synthesized samples.

2.1.5. The ^{27}Al, ^{29}Si, and ^{31}P MAS NMR Spectra of SAPO-34 Zeolite

As Brønsted acidity is particularly associated with the isolated Si coordination environment of Si(4Al), solid-state nuclear magnetic resonance (NMR) has been extensively used to characterise the coordination environment in SAPO-34 zeolites [29]. Figure 5 shows the ^{27}Al, ^{29}Si, and ^{31}P solid-state, magic-angle spinning (MAS) NMR spectra of the as-synthesised SAPO-34 samples. ^{27}Al NMR shows a typical NMR peak at 45 ppm, which can be assigned to the tetrahedrally coordinated framework of Al atoms [18]. Additionally, the signal resonance of tetrahedral Al in the SAPO-34 framework in SP-0.6 is stronger than that of the other two samples, indicating its higher crystallinity. The ^{27}Al signal resonance at −10 ppm, which can be assigned to the six-coordinated Al derived from the tetrahedral Al species, coordinates further with two water molecules; this suggests the existence of extra-framework species in the as-synthesised SAPO-34 samples [22,30]. The presence of a ^{27}Al signal resonance at 10 ppm, which corresponds to pentacoordinated Al atoms, is associated with the coordination of tetrahedral Al atoms in the framework with water molecules [31]. The resonance signals at 10 ppm become weaker with increasing Si content, indicating that the interaction between the four-coordinated Al species and water molecules is weakened, while the interaction between the tetrahedral Al species and Si atoms is facilitated. Therefore, the Si coordination environments of the samples were investigated further using solid-state ^{29}Si MAS NMR spectroscopy.

As shown in Figure 5b, the ^{29}Si spectrum of SP-0.2 shows a major NMR peak at −89 ppm, which can be assigned to the typical Si(4Al) coordination environments in the SAPO framework [9,11,12,18]; the weak peaks at approximately −95, −100, −105, and −110 ppm indicate the presence of diverse Si species such as Si(3Al), Si(2Al), Si(1Al), and

Si(0Al). Moreover, the various chemical environments in the framework of SP-0.2 are formed accordingly [9,21]. The ^{29}Si spectrum of SP-0.6 clearly shows a dominant peak at -88 ppm, and this resonance peak becomes stronger and narrower than that of SP-0.2; this indicates the dominance of the Si(4Al) species because of the incorporation of numerous Si atoms into the SAPO-34 framework through the SM2 substitution mechanism [13]. This result is in good agreement with the high crystallinity and high acid content of the SP-0.6 sample. The ^{29}Si NMR spectra of SP-1.0 changes significantly and shows a broadened resonance region. The intensity and integral area of the resonance peak at approximately -90 and -110 ppm are almost similar, suggesting that SP-0.6 contains both Si(4Al) species in the framework and silica islands owing to the Si-atom incorporation into the framework via a combination of the SM2 and SM3 substitution mechanisms. This phenomenon is consistent with the high-silica-content characteristic of SAPO-34 samples synthesised via hydrothermal crystallisation [15]. The SiO_2/Al_2O_3 molar ratio in the precursor mixture is noted to have a crucial impact on the mechanisms of Si-atom's incorporation into the framework, with a threshold ratio of 0.6 being required for the two substitution mechanisms to occur.
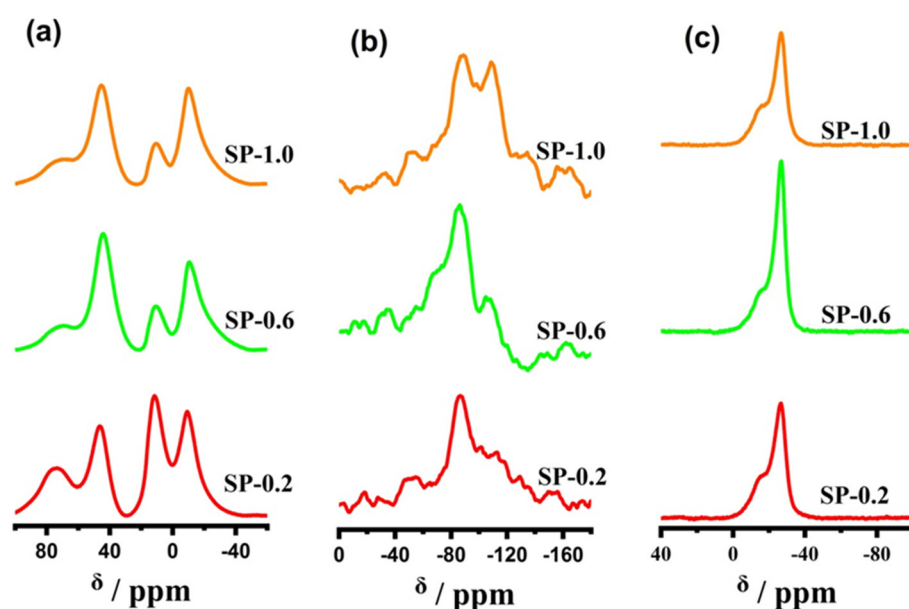

Figure 5. (**a**) ^{27}Al; (**b**) ^{29}Si NMR; (**c**) ^{31}P spectra of as-synthesized SAPO-34 samples.

The ^{31}P NMR spectrum of the as-synthesised SAPO-34 samples exhibits a strong single resonance at -28 ppm and weaker shoulder signals at -15 ppm; the former can be attributed to the formation of P(4Al) species via the bonding of four-coordinated phosphorus atoms and four aluminium atoms [14], and the latter correspond to the formation of partially hydrated $P(OAl)_x(H_2O)_y$ species through the coordination of phosphorus atoms with several water molecules [29]. Sample SP-0.6 shows the strongest resonance peaks at -28 ppm compared with those of the other two samples, suggesting the dominance of the P(4Al) species; this is in good agreement with the XRD and NH_3-TPD results.

2.2. Catalytic Performance of As-Synthesized SAPO-34 Zeolite

The effects of the SiO_2/Al_2O_3 ratio on the catalytic performance of SAPO-34 zeolite catalysts for the cracking of 1-butene were subsequently investigated (Table 4 and Figure 6). The conversion of 1-butene on SAPO-34 catalysts is noted to first increase, and subsequently decrease with an increase in the SiO_2/Al_2O_3 ratio; the optimal conversion of 82.8% corresponds to the SP-0.6 sample. The combined yield of ethene and propene also clearly change with an increase in the SiO_2/Al_2O_3 ratio. As shown in Figure 6b, the yield of ethene and propene as a function of the SiO_2/Al_2O_3 ratio with the investigated catalysts shows a similar volcanic curve to that shown in Figure 6a, with the highest yield of the

light olefin (51.6%) being obtained with the SP-0.6 catalyst. Meanwhile, we found that the catalytic performance of the solvent-free synthesized SP-0.6 samples is comparable to that of commercial SAPO-34. (Table S1, Figure S2, Supplementary Information) The selectivity to ethene is noted to increase with increasing SiO_2/Al_2O_3 ratios, reach a maximum of 18.9% for the SP-0.6 sample, and subsequently decrease with a further increase in the SiO_2/Al_2O_3 ratio. The selectivity to propene decreases gradually as the SiO_2/Al_2O_3 ratio increases from 0.2 to 0.6, with the highest value (62.1%) corresponding to the SP-0.2 sample. At a SiO_2/Al_2O_3 ratio greater than 0.6, the selectivity to propene slightly increases with increasing SiO_2/Al_2O_3 ratios. The total selectivity towards ethene and propene decreases with increasing SiO_2/Al_2O_3 ratios, with the highest light olefins selectivity (74.7%) being obtained for the SP-0.2 sample; the selectivity to light olefins stabilises at ~62.5%, with a further increase in the SiO_2/Al_2O_3 ratio. These results reveal the crucial effect of SiO_2/Al_2O_3 on the activity and selectivity of SAPO-34 catalysts in the catalytic cracking of 1-butene; this is because the number and distribution of Si atoms in the framework can directly affect the acidic properties of the resulting SAPO-34 samples [10,12]. The effect of the SiO_2/Al_2O_3 ratio on the hydrogen transfer coefficient (HTC) was also thoroughly investigated (Table 4). The HTC of the SAPO-34 catalysts was noted to first increase and subsequently decrease with increasing SiO_2/Al_2O_3 ratios; a maximum HTC of 0.65 was obtained for the SP-0.6 sample, indicating the tendency of propene to undergo a hydrogen transfer reaction, which results in a decrease in selectivity. The 1-butene cracking reaction network is known to be relatively complicated, with various side reactions accompanying the primary cracking reaction. The influence of the number of acid sites in the SAPO-34 catalysts on catalytic activity and propene selectivity were also examined. Figure 6d indicates that the catalytic cracking activity of the SAPO-34 catalysts is strongly dependent on the concentration of acid sites, with a noteworthy positive linear correlation between the total acid content and catalytic activity. By contrast, the relationship between propene selectivity and the total acid content shows significant negative linear correlations, indicating that a high concentration of acid sites is also unfavourable for the catalytic cracking of 1-butene. Possible reasons for this behaviour may be the occurrence of side reactions, acceleration of coke deposition, and reduction in the catalyst lifetime and light olefin selectivity [23,32,33].

Table 4. Product distribution of 1-butene catalytic cracking over as-synthesized SAPO-34 samples.

Catalysts	Conversion (wt%)	Selectivity (wt%)						HTC [1]
		$CH_4 + C_2H_6$	H_2	C_2H_4	C_3H_6	$C_3H_8 + C_4H_{10}$	C_5+	
SP-0.2	42.2	0.5	0.2	12.6	62.1	9.9	14.6	0.16
SP-0.4	52.7	0.9	0.2	15.6	56.2	14.8	12.2	0.26
SP-0.6	82.8	2.1	0.5	18.9	43.3	28.2	7.0	0.65
SP-0.8	75.0	1.1	0.4	14.8	47.2	19.1	16.9	0.40
SP-1.0	74.1	0.9	0.4	14.7	47.8	18.2	16.7	0.38

Reaction conditions: WHSV = 1.5 h^{-1}, P = 0.1 Mpa, T = 500 °C, TOS = 10 min; [1] HTC: The hydrogen transfer coefficient was defined as the ratio of selectivity of C_3H_8 plus C_4H_{10} with respect to selectivity of C_3H_6.

Figure 7 shows the time-on-stream (TOS) evolution of the conversion of 1-butene, yield of ethene and propene, and selectivity of ethene and propene. The conversion of 1-butene based on all the SAPO-34 catalysts is noted to decrease sharply with an increase in the TOS, indicating the rapid deactivation of SAPO-34 catalysts during the catalytic cracking of 1-butene; this may be attributed to the blockage of micropores by the coke formed within the cavities (cages) between the crystalline channels [32]. The SAPO-34 catalysts are almost completely deactivated by the coke deposits after a TOS of 100 min. The rapid deactivation of SAPO-34 in the cracking of 1-butene has also been reported [32,33]. In addition, the SP-1.0 catalyst shows a slow coke deactivation, which is attributed to its large mesopores and suitable number of acid sites. The coke contents of the spent SP-0.6 catalyst and the commercial SAPO-34 were further characterized by thermogravimetric analysis (Figure S3). From the TG curves of SP-0.6 sample and commercial SAPO-34, which

were used in the catalytic cracking of 1-butene for 150 min (Figure S3), the amounts of the formed coke that were deposited on the two spent catalysts were similar (about 15%). Therefore, it is an important challenge to improve the catalyst stability of SAPO-34 against coke deactivation. Therefore, an SAPO-34 catalyst was designed by adjusting the acidity with slow coke deactivation to improve the catalyst lifetime.
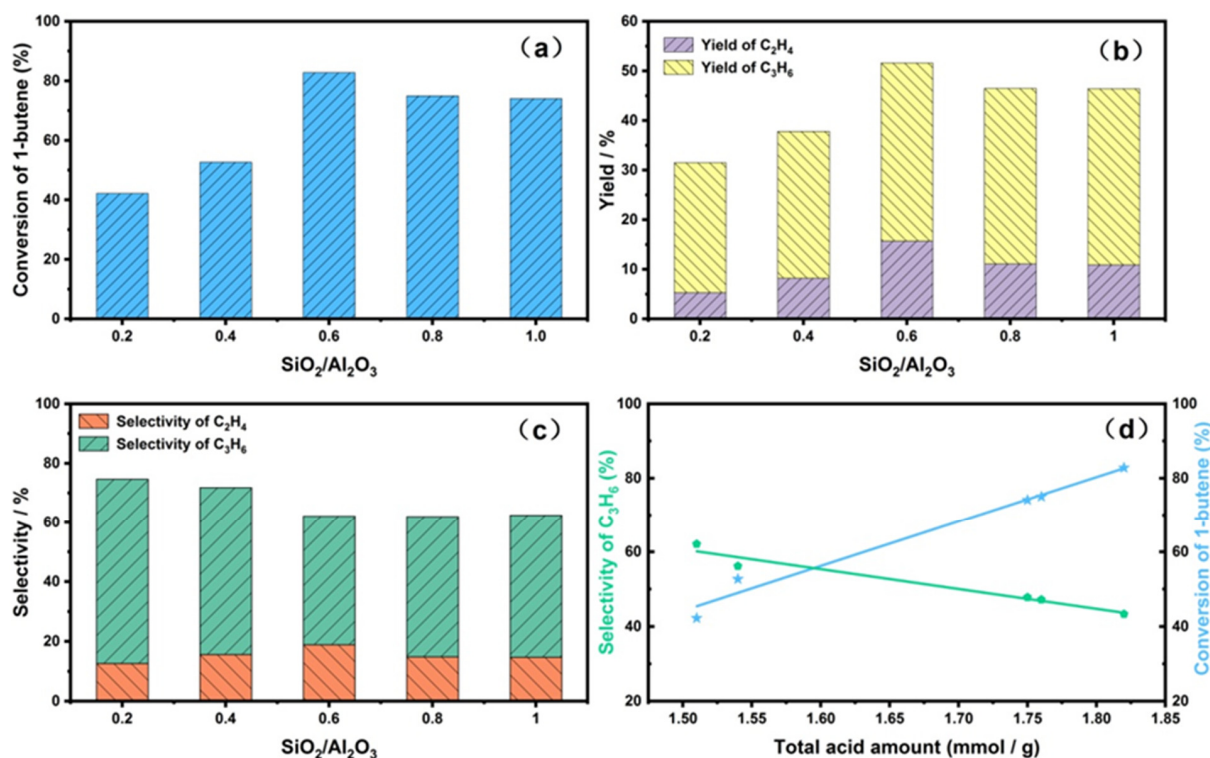

Figure 6. (**a**) Conversion of 1-butene; (**b**) Yield of ethene, propene; (**c**) Selectivity of ethene, propene a function of the SiO_2/Al_2O_3 over as-synthesized SAPO-34 zeolite catalysts; (**d**) Selectivity of propene and conversion of 1-butene as a function of total acid amount over as-synthesized SAPO-34 zeolite catalysts.
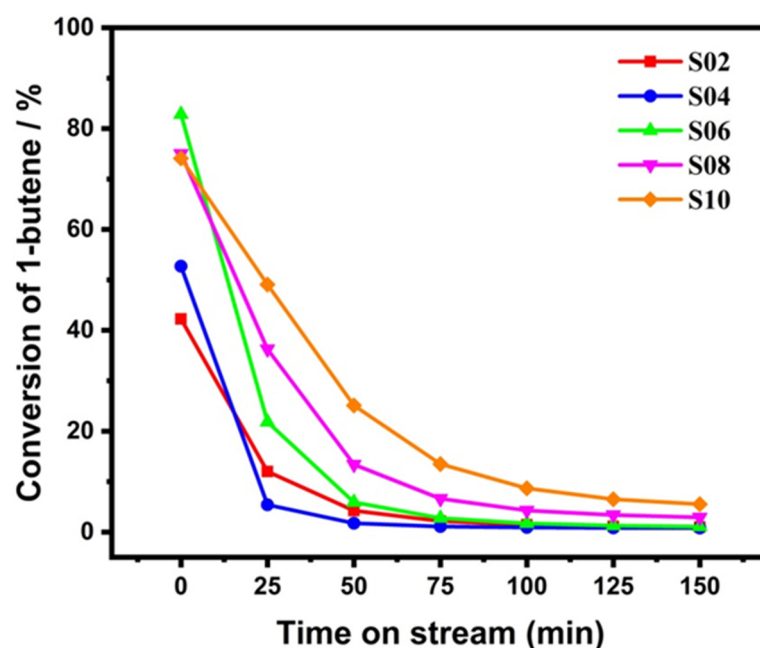

Figure 7. The conversion of 1-butene for SAPO-34 catalysts with time on stream. Reaction conditions: WHSV = 1.5 h^{-1}, P = 0.1 Mpa, T = 500 °C.

3. Materials and Methods

3.1. Chemicals

Boehmite, fumed silica and tetraethylammonium hydroxide (TEAOH, 25wt%) were supplied from Macklin Chemical Co., Ltd. (Shanghai, China). Morpholine (99%), and $NH_4H_2PO_4$ (99%) were obtained from Sinopharm Chemical Reagent Co., Ltd. (Shanghai, China). All chemicals were used without further purification. The commercial SAPO-34 (the molar ratio of SiO_2/Al_2O_3 is 0.5) was obtained from Naikai Catalyst Co., Ltd. (Tianjin, China).

3.2. Synthesis of SAPO-34 Zeolite

The SAPO-34 zeolite samples were synthesized by the improved solvent-free synthesis method. To prepare the SAPO-34 zeolite, boehmite, fumed silica and $NH_4H_2PO_4$ were used as an aluminum source, silicon source and phosphorus source, respectively. Morpholine and tetraethylammonium hydroxide were used as a composite template. The starting materials had a molar ratio of 1.0 Al_2O_3:0.5 P_2O_5:x SiO_2:2.4 MOR:0.24 TEAOH, where x is 0.0, 0.2, 0.4, 0.6, 0.8 and 1.0, respectively. Firstly, a certain amount of fumed silica, boehmite and $NH_4H_2PO_4$ was mixed. Then, morpholine and TEAOH were added dropwise. After grinding at room temperature for 3 h, the mixture was transferred to an autoclave, then crystallized using a Teflon-lined stainless-steel vessel at 200 °C for 24 h. The obtained product was washed thoroughly with DI water and dried at 80 °C. The powder samples were calcined in a muffle furnace at 600 °C for 6 h in air to remove the template agents. The as-synthesized these SAPO-34 samples at different x values were noted as SP-0.0, SP-0.2, SP-0.4, SP-0.6, SP-0.8 and SP-1.0, respectively.

3.3. Catalyst Characterization

The crystallinity and phase purity of the samples were characterized by powder X-ray diffraction on a RIGAKU Ultima IV Powder Diffractometer equipped with a Cu Kα (λ = 0.15406 nm) radiation with a Nickel filter operating at 40 KV and 40 mA, at a scanning rate of 2°/min from 5° to 40°. The crystal size and morphology of the samples were observed with scanning electron microscopy (SEM) on a HITACHI SU8020 instrument with an accelerating voltage of 3 KV. Chemical compositions were determined with X-ray fluorescence (XRF) analysis, carried out on a Thermo Scientific ARL ADVANT'X InliPower. The Nitrogen adsorption–desorption isotherms were measured at liquid N_2 temperature (−196 °C) with a Micromeritics ASAP-2460 instrument after activation in vacuum at 300 °C for 6 h. The specific surface area (S_{BET}) was determined by applying the Brunauer–Emmett–Teller (BET) equation. The external surface area (S_{ext}) and micropore volume (V_{micro}) were evaluated by the t-plot method. Pore size distribution and mesopore volume (V_{meso}) were evaluated by applying the Barrett–Joyner–Halenda (BJH) method to the adsorption branch of the isotherm. The solid-state MAS NMR spectra were performed on a Bruker Avance III 600 spectrometer at room temperature. The kaolinite, hydrated $Al(NO_3)_3$ and a queous 85% H_3PO_4 were used as external references for the ^{29}Si, ^{27}Al and ^{31}P NMR chemical shifts, respectively. The temperature-programmed desorption of ammonia (NH_3-TPD) was carried out on a Micrometitics AutoChem II 2920 chemical adsorption instrument. Before NH_3-TPD measurements, the catalyst (100 mg, 40–60 mesh) was activated by heating in a N_2 flow outgassed at 600 °C for 1 h. After cooling to 100 °C, NH_3 adsorption was carried out. After saturation, the catalyst was purged by N_2 flow at 100 °C for 2 h to remove the physically adsorbed NH_3 from the sample. Then, the remaining strongly adsorbed NH_3 was desorbed by heating the sample to 700 °C with a heating rate of 10 °C/min, and the amount of desorbed NH_3 was simultaneously monitored by thermal conductivity detector (TCD). Thermogravimetric analysis was performed on a NETZSCH STA449F5 Jupiter TGA/DSC instrument to determine the total amount of coke. The experiment was carried out with about 10 mg coked catalyst under an 80 mL/min air flow, and the ramp rate was 10 °C/min.

3.4. Catalytic Activity Evaluation

The catalytic cracking of n-butene reaction was carried out in a continuous flow fixed-bed tubular quartz reactor (10 mm i.d.) at atmospheric pressure, with a thermocouple in the center of the catalyst bed to measure the reaction temperature. Prior to the catalytic reaction, the catalyst (500 mg) was pretreated at 500 °C for 1 h with a nitrogen stream (40 mL/min), followed by the introduction of 1-butene mixed with N_2 into the reactor (N_2/1-C_4H_8 = 7.82, mole ratio, analyzed by GC). Reaction products were analyzed on-line by an Agilent GC-7890B gas chromatograph equipped with an FID detector with an HP-PLOT/Al_2O_3 capillary column (50 m × 0.32 mm × 8 μm) and an HP-INOWax column (30 m, 0.32 mm, 0.5 μm). It is generally accepted that the 1-butene rapidly reaches thermodynamic equilibrium at the reactor inlet in the catalytic cracking of 1-butene reaction, and thus, all butenes are considered as part of the feed. Then, the 1-butene conversion, selectivity to products and yield of products were calculated by the following respective formulas. When m(1-butene)$_{in}$ and m(1-butene)$_{out}$ are the mass fraction of 1-butene before and after the reaction, m(C_xH_y) is the mass fraction of products, and $\sum m(C_iH_j)$ is the sum of the mass fraction of products. The abbreviation for the hydrogen transfer coefficient is HTC, which is defined as the ratio of selectivity of C_3H_8 plus C_4H_{10} with respect to the selectivity of C_3H_6.

$$\text{Conversion of 1–butene} = \frac{\text{m(1–butene)}_{in} - \text{m(1–butene)}_{out}}{\text{m(1–butene)}_{in}} \times 100\% \qquad (1)$$

$$\text{Selectivity to } C_xH_y = \frac{mC_xH_y}{\sum m(C_iH_j)} \times 100\% \qquad (2)$$

$$\text{Yield of } C_xH_y = \text{Selectivity to } C_xH_y \times \text{Conversion of 1–butene} \times 100\% \qquad (3)$$

4. Conclusions

An environmentally benign process was developed for the facile synthesis of SAPO-34 zeolites with tunable SiO_2/Al_2O_3 molar ratios through a solvent-free route. The crystal size, textural structure, acidity, and Si chemical coordination environment of the resulting SAPO-34 crystals are determined by the silicon content in the raw materials mixture composition of the dual template system. With an increase in the SiO_2/Al_2O_3 molar ratio, the crystal size of SAPO-34 increased, and the specific surface area, pore volume, and acidic content first increased, and subsequently slightly decreased. Moreover, the Si chemical coordination environment in the SAPO-34 framework varied with the SiO_2/Al_2O_3 ratio. A threshold ratio (SiO_2/Al_2O_3 = 0.6) was noted to exist for the Si content in the raw material mixture. When the SiO_2/Al_2O_3 ratio was higher than this threshold, Si atoms were incorporated into the framework via a combination of the SM2 and SM3 substitution mechanisms. Then, the silicon islands were formed and produced no new acid sites, which was consistent with the Si incorporation mechanisms in the SAPO-34 zeolite synthesised by the hydrothermal method. The tunable acidity of SAPO-34 resulted in flexible adjustments to its catalytic performance for the catalytic cracking of 1-butene. The highest conversion of 1-butene (82.8%) and yield of light olefins (51.6%) were obtained over the SP-0.6 catalyst, which could be attributed to the presence of a higher number of acid sites in SP-0.6 than in the other samples. This solvent-free route provides a facile strategy for the effective scale-up of SAPO-34 zeolites' production, and will be crucial for industrial production in the future.

Supplementary Materials: The following are available online at https://www.mdpi.com/article/10.3390/catal11070835/s1, Figure S1: The XRD pattern (left) and SEM image (right) of commercial SAPO-34. Figure S2: The conversion of 1-butene for commercial SAPO-34 catalysts with time on stream. Reaction conditions: WHSV = 1.5 h−1, P = 0.1 Mpa, T = 500 °C. Figure S3: TG profiles of coked SP-0.6 catalyst and commercial SAPO-34 at 150 min. Table S1: Product distribution of 1-butene catalytic cracking over commercial SAPO-34.

References

1. Sun, Q.; Xie, Z.; Yu, J. The state-of-the-art synthetic strategies for SAPO-34 zeolite catalysts in methanol-to-olefin conversion. *Natl. Sci. Rev.* **2018**, *5*, 542–558. [CrossRef]
2. Peng, S.C.; Gao, M.B.; Li, H.; Yang, M.; Ye, M.; Liu, Z.M. Control of Surface Barriers in Mass Transfer to Modulate Methanol-to-Olefins Reaction over SAPO-34 Zeolites. *Angew. Chem. Int. Ed.* **2020**, *59*, 21945–21948. [CrossRef]
3. Gao, M.B.; Li, H.; Liu, W.J.; Xu, Z.C.; Peng, S.C.; Yang, M.; Ye, M.; Liu, Z.M. Imaging spatiotemporal evolution of molecules and active sites in zeolite catalyst during methanol-to-olefins reaction. *Nat. Commun.* **2020**, *11*, 3641. [CrossRef] [PubMed]
4. Dusselier, M.; Davis, M.E. Small-Pore Zeolites: Synthesis and Catalysis. *Chem. Rev.* **2018**, *118*, 5265–5329. [CrossRef] [PubMed]
5. Moliner, M.; Martinez, C.; Corma, A. Synthesis Strategies for Preparing Useful Small Pore Zeolites and Zeotypes for Gas Separations and Catalysis. *Chem. Mater.* **2014**, *26*, 246–258. [CrossRef]
6. Huang, Y.; Wang, L.; Song, Z.N.; Li, S.G.; Yu, M. Growth of High-Quality, Thickness-Reduced Zeolite Membranes towards N_2/CH_4 Separation Using High-Aspect-Ratio Seeds. *Angew. Chem. Int. Ed.* **2015**, *54*, 10843–10847. [CrossRef] [PubMed]
7. Lin, L.F.; Qiu, C.F.; Zhuo, Z.X.; Zhang, D.W.; Zhao, S.F.; Wu, H.H.; Liu, Y.M.; He, M.Y. Acid strength controlled reaction pathways for the catalytic cracking of 1-butene to propene over ZSM-5. *J. Catal.* **2014**, *309*, 136–145. [CrossRef]
8. Zang, Y.H.; Dong, X.F.; Ping, D.; Geng, J.M.; Dang, H.F. Green routes for the synthesis of hierarchical HZSM-5 zeolites with low SiO_2/Al_2O_3 ratios for enhanced catalytic performance. *Catal. Commun.* **2018**, *113*, 51–54. [CrossRef]
9. Minova, I.B.; Barrow, N.S.; Sauerwein, A.C.; Naden, A.B.; Cordes, D.B.; Slawin, A.M.Z.; Schuyten, S.J.; Wright, P.A. Silicon redistribution, acid site loss and the formation of a core–shell texture upon steaming SAPO-34 and their impact on catalytic performance in the Methanol-to-Olefins (MTO) reaction. *J. Catal.* **2021**, *395*, 425–444. [CrossRef]
10. Pimerzin, A.; Savinov, A.; Vutolkina, A.; Makova, A.; Glotov, A.; Vinokurov, V.; Pimerzin, A. Transition Metal Sulfides- and Noble Metal-Based Catalysts for N-Hexadecane Hydroisomerization: A Study of Poisons Tolerance. *Catalysts* **2020**, *10*, 594. [CrossRef]
11. Tan, J.; Liu, Z.M.; Bao, X.H.; Liu, X.C.; Han, X.W.; He, C.Q.; Zhai, R.S. Crystallization and Si incorporation mechanisms of SAPO-34. *Micropor. Mesopor. Mater.* **2002**, *53*, 97–108. [CrossRef]
12. Sena, F.C.; de Souza, B.F.; de Almeida, N.C.; Cardoso, J.S.; Fernandes, L.D. Influence of framework composition over SAPO-34 and MeAPSO-34 acidity. *Appl. Catal. A Gen.* **2011**, *406*, 59–62. [CrossRef]
13. Xu, L.; Du, A.P.; Wei, Y.X.; Wang, Y.L.; Yu, Z.X.; He, Y.L.; Zhang, X.Z.; Liu, Z.M. Synthesis of SAPO-34 with only Si(4Al) species: Effect of Si contents on Si incorporation mechanism and Si coordination environment of SAPO-34. *Micropor. Mesopor. Mater.* **2008**, *115*, 332–337. [CrossRef]
14. Gao, B.B.; Yang, M.; Qiao, Y.Y.; Li, J.Z.; Xiang, X.; Wu, P.F.; Wei, Y.X.; Xu, S.T.; Tian, P.; Liu, Z.M. A low-temperature approach to synthesize low-silica SAPO-34 nanocrystals and their application in the methanol-to-olefins (MTO) reaction. *Catal. Sci. Technol.* **2016**, *6*, 7569–7578. [CrossRef]
15. Izadbakhsh, A.; Farhadi, F.; Khorasheh, F.; Sahebdelfar, S.; Asadi, M.; Yan, Z.F. Key parameters in hydrothermal synthesis and characterization of low silicon content SAPO-34 molecular sieve. *Micropor. Mesopor. Mater.* **2009**, *126*, 1–7. [CrossRef]
16. Wu, Q.; Meng, X.; Gao, X.; Xiao, F.S. Solvent-Free Synthesis of Zeolites: Mechanism and Utility. *Acc. Chem. Res.* **2018**, *51*, 1396–1403. [CrossRef]
17. Zhu, Q.; Wang, Y.; Wang, L.; Yang, Z.; Wang, L.; Meng, X.; Xiao, F.-S. Solvent-free crystallization of ZSM-5 zeolite on SiC foam as a monolith catalyst for biofuel upgrading. *Chin. J. Catal.* **2020**, *41*, 1118–1124. [CrossRef]
18. Jin, Y.; Sun, Q.; Qi, G.; Yang, C.; Xu, J.; Chen, F.; Meng, X.; Deng, F.; Xiao, F.-S. Solvent-Free Synthesis of Silicoaluminophosphate Zeolites. *Angew. Chem. Int. Ed.* **2013**, *52*, 9172–9175. [CrossRef] [PubMed]
19. Jin, Y.; Chen, X.; Sun, Q.; Sheng, N.; Liu, Y.; Bian, C.; Chen, F.; Meng, X.; Xiao, F.-S. Solvent-Free Syntheses of Hierarchically Porous Aluminophosphate-Based Zeolites with AEL and AFI Structures. *Chem. Eur. J.* **2014**, *20*, 17616–17623. [CrossRef]
20. Meng, X.J.; Xiao, F.S. Green Routes for Synthesis of Zeolites. *Chem. Rev.* **2014**, *114*, 1521–1543. [CrossRef]

21. Wang, T.; Yang, C.; Li, S.; Yu, G.; Liu, Z.; Wang, H.; Gao, P.; Sun, Y. Solvent-Free Synthesis of Mg-Incorporated Nanocrystalline SAPO-34 Zeolites via Natural Clay for Chloromethane-to-Olefin Conversion. *ACS Sustain. Chem. Eng.* **2020**, *8*, 4185–4193. [CrossRef]

22. Liu, Z.; Ren, S.; Yu, X.; Chen, X.; Wang, G.; Wu, X.; Yu, G.; Qiu, M.; Yang, C.; Sun, Y. Melting-assisted solvent-free synthesis of hierarchical SAPO-34 with enhanced methanol to olefins (MTO) performance. *Catal. Sci. Technol.* **2018**, *8*, 423–427. [CrossRef]

23. Hu, B.; Mao, G.L.; Wang, D.K.; Fu, Y.D.; Wang, B.H.; Luo, M.J. Conversion and coking of olefins on SAPO-34. *Catal. Sci. Technol.* **2017**, *7*, 5785–5794. [CrossRef]

24. Blay, V.; Louis, B.; Miravalles, R.; Yokoi, T.; Peccatiello, K.A.; Clough, M.; Yilmaz, B. Engineering Zeolites for Catalytic Cracking to Light Olefins. *ACS Catal.* **2017**, *7*, 6542–6566. [CrossRef]

25. Sattler, J.J.H.B.; Ruiz-Martinez, J.; Santillan-Jimenez, E.; Weckhuysen, B.M. Catalytic dehydrogenation of light alkanes on metals and metal oxides. *Chem. Rev.* **2014**, *114*, 10613–10653. [CrossRef] [PubMed]

26. Sheng, J.; Yan, B.; Lu, W.D.; Qiu, B.; Gao, X.Q.; Wang, D.; Lu, A.H. Oxidative dehydrogenation of light alkanes to olefins on metal-free catalysts. *Chem. Soc. Rev.* **2021**, *50*, 1438–1468. [CrossRef]

27. Zhong, L.S.; Yu, F.; An, Y.L.; Zhao, Y.H.; Sun, Y.H.; Li, Z.J.; Lin, T.J.; Lin, Y.J.; Qi, X.Z.; Dai, Y.Y.; et al. Cobalt carbide nanoprisms for direct production of lower olefins from syngas. *Nature* **2016**, *538*, 84–87. [CrossRef]

28. Jiao, F.; Li, J.J.; Pan, X.L.; Xiao, J.P.; Li, H.B.; Ma, H.; Wei, M.M.; Pan, Y.; Zhou, Z.Y.; Li, M.R.; et al. Selective conversion of syngas to light olefins. *Science* **2016**, *351*, 1065–1068. [CrossRef]

29. Watanabe, Y.; Koiwai, A.; Takeuchi, H.; Hyodo, S.A.; Noda, S. Multinuclear NMR Studies on the Thermal Stability of SAPO-34. *J. Catal.* **1993**, *143*, 430–436. [CrossRef]

30. Li, Z.; Martínez-Triguero, J.; Concepción, P.; Yu, J.; Corma, A. Methanol to olefins: Activity and stability of nanosized SAPO-34 molecular sieves and control of selectivity by silicon distribution. *Phys. Chem. Chem. Phys.* **2013**, *15*, 14670. [CrossRef] [PubMed]

31. Blackwell, C.S.; Patton, R.L. Aluminum-27 and Phosphorus-31 Nuclear Magnetic Resonance Studies of Aluminophosphate Molecular Sieves. *J. Phys. Chem.* **1984**, *88*, 6135–6139. [CrossRef]

32. Epelde, E.; Ibanez, M.; Aguayo, A.T.; Gayubo, A.G.; Bilbao, J.; Castano, P. Differences among the deactivation pathway of HZSM-5 zeolite and SAPO-34 in the transformation of ethylene or 1-butene to propylene. *Micropor. Mesopor. Mater.* **2014**, *195*, 284–293. [CrossRef]

33. Epelde, E.; Ibáñez, M.; Valecillos, J.; Aguayo, A.T.; Gayubo, A.G.; Bilbao, J.; Castaño, P. SAPO-18 and SAPO-34 catalysts for propylene production from the oligomerization-cracking of ethylene or 1-butene. *Appl. Catal. A Gen.* **2017**, *547*, 176–182. [CrossRef]